PET digitization chain for Monte Carlo simulation in GATE

Julien Salvadori, Antoine Merlet, Benoit Presles, Jorge Cabello, Kuan-Hao Su, Alexandre Cochet, Ane Etxebeste, Jean-Marc Vrigneaud, David Sarrut

Physics in Medicine & Biology

PAPER • **OPEN ACCESS**

PET digitization chain for Monte Carlo simulation in GATE

To cite this article: Julien Salvadori *et al* 2024 *Phys. Med. Biol.* **69** 165013

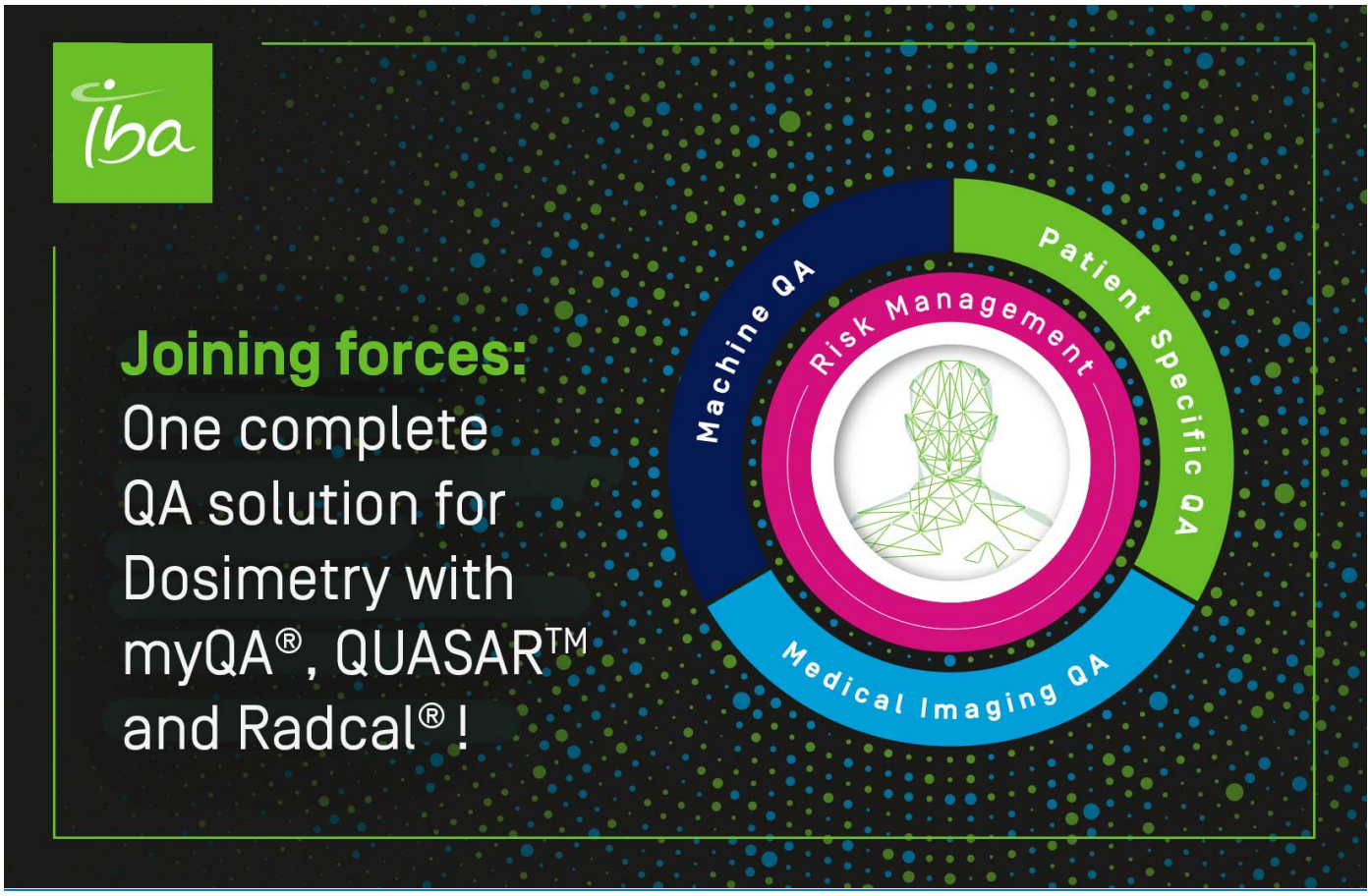

IOP Publishing Phys. Med. Biol. 69 (2024) 165013 https://doi.org/10.1088/1361-6560/ad638c

Physics in Medicine & Biology

IPEM Institute of Physics and Engineering in Medicine

OPEN ACCESS

RECEIVED
22 April 2024

REVISED
1 July 2024

ACCEPTED FOR PUBLICATION
15 July 2024

PUBLISHED
2 August 2024

PAPER

PET digitization chain for Monte Carlo simulation in GATE

Julien Salvadori[1,*], **Antoine Merlet**[2], **Benoit Presles**[2], **Jorge Cabello**[3], **Kuan-Hao Su**[4], **Alexandre Cochet**[2,5], **Ane Etxebeste**[6], **Jean-Marc Vrigneaud**[2,5] and **David Sarrut**[6]

[1] Groupement de Coopération Sanitaire, Institut de Cancérologie Strasbourg Europe (ICANS), Nuclear medicine, Strasbourg, France
[2] Institut de Chimie Moléculaire de l'Université de Bourgogne (ICMUB), UMR CNRS 6302, University of Burgundy, Dijon, France
[3] Siemens Medical Solutions, USA, Inc., Knoxville, TN, United States of America
[4] GE Healthcare, Waukesha, WI, United States of America
[5] Department of Nuclear Medicine, Georges-François Leclerc Cancer Centre, Dijon, France
[6] Université de Lyon, CREATIS; CNRS UMR5220, Inserm U1044, INSA-Lyon; Université Lyon 1, Centre Léon Bérard, France
[*] Author to whom any correspondence should be addressed.

E-mail: j.salvadori89@gmail.com

Keywords: PET, GATE, Monte-Carlo simulation, digitizer

Abstract

Objective. We introduce a versatile methodology for the accurate modelling of PET imaging systems via Monte Carlo simulations, using the Geant4 application for tomographic emission (GATE) platform. Accurate Monte Carlo modelling involves the incorporation of a complete analytical signal processing chain, called the digitizer in GATE, to emulate the different count rates encountered in actual positron emission tomography (PET) systems. *Approach*. The proposed approach consists of two steps: (1) modelling the digitizer to replicate the detection chain of real systems, covering all available parameters, whether publicly accessible or supplied by manufacturers; (2) estimating the remaining parameters, i.e. background noise level, detection efficiency, and pile-up, using optimisation techniques based on experimental single and prompt event rates. We show that this two-step optimisation reproduces the other experimental count rates (true, scatter, and random), without the need for additional adjustments. This method has been applied and validated with experimental data derived from the NEMA count losses test for three state-of-the-art SiPM-based time-of-flight (TOF)-PET systems: Philips Vereos, Siemens Biograph Vision 600 and GE Discovery MI 4-ring. *Main results*. The results show good agreement between experiments and simulations for the three PET systems, with absolute relative discrepancies below 3%, 6%, 6%, 7% and 12% for prompt, random, true, scatter and noise equivalent count rates, respectively, within the 0–10 kBq·ml^{-1} activity concentration range typically observed in whole-body ^{18}F scans. *Significance*. Overall, the proposed digitizer optimisation method was shown to be effective in reproducing count rates and NECR for three of the latest generation SiPM-based TOF-PET imaging systems. The proposed methodology could be applied to other PET scanners.

1. Introduction

GATE (Sarrut *et al* 2021, 2022) is an open-source platform based on the Geant4 engine (Allison *et al* 2016) for Monte Carlo simulations in medical imaging and radiotherapy. It is based on Geant4's functionalities to support the design of positron emission tomography (PET) systems, enabling geometric modelling of detection systems and the management of detector responses via an analytical signal processing chain known as the 'digitizer'. This digitizer plays an essential role in shaping the signals, determining interaction timestamps and positions, modelling timing and energy resolutions, accounting for detector saturation effects, and managing the pulse-processing logic essential for the selection and coupling of single events into coincidences. The determination of digitizer parameters is crucial for accurate simulations, especially at low activity levels where background noise predominates, and at high activity levels where saturation effects, such as dead time and pile-up, significantly affect the results.

Obtaining specific parameter settings for digitizers directly from manufacturers often poses significant challenges. These difficulties arise from proprietary concerns, limited accessibility, and strict non-disclosure policies that manufacturers enforce, complicating the retrieval of essential data needed for accurate digitizer modelling. This context underscores the necessity for developing robust optimisation methods that can independently establish these parameters.

Several clinical PET systems from leading manufacturers—Philips Healthcare, Siemens Healthineers, and General Electric Healthcare (GE) - have been modelled using GATE/Geant4, including Philips Allegro (Lamare *et al* 2006), Gemini TF (Trindade *et al* 2012), and Vereos (Salvadori *et al* 2020); Siemens Biograph 6 (Gonias *et al* 2007), DUO (Nikolopoulos *et al* 2013), mMR (Aklan *et al* 2015) and Vision (Zein *et al* 2020); and GE Discovery LS (Schmidtlein *et al* 2005), RX (Geramifar *et al* 2011), and MI (Kalaitzidis *et al* 2022, Tiwari *et al* 2022, Merlet *et al* 2024). A comprehensive review of GATE-modelled PET systems is provided in Sarrut *et al* (2021).

One way to set the values for the digitizer parameters is to apply an optimisation process on most variables, including the known ones. This method was recently introduced by Herald *et al* (2022), in which evolutionary algorithms are used to optimise all the digitizer parameters simultaneously. This method produces remarkable results but requires significant computational resources due to the extensive parameter set.

Another approach stem from the work of Guez *et al* (2008), combining manufacturer-provided values with models that fit experimental count rates. This approach was further refined by Salvadori *et al* (2020) for the Philips Vereos PET system and extended by Merlet *et al* (2024) to the GE Discovery MI 4-ring PET system. Although these studies were performed with slight variations in optimisation methodology, they both showed the proper GATE modelling of their respective PET system. This indicates that it may be possible to develop a generic (system-independent) optimisation method for the digitizer.

In this context, we propose a generic method to design and evaluate the digitizer, using experimental data from the NEMA count losses and scatter fraction protocol, hereinafter called 'NEMA count losses'. We apply this methodology to three state-of-the-art time-of-flight (TOF) PET systems equipped with silicon photomultipliers (SiPM) : Philips Vereos, Siemens Biograph Vision 600 (Vision 600) and GE Discovery MI 4-ring (DMI 4-ring).

2. Material and methods

This section details the three studied PET systems as well as the experimental data required for digitizer optimisation and validation. Subsequently, we describe the Monte Carlo simulation model and the proposed digitizer optimisation procedure.

2.1. Geometry of the three PET systems

Specifications of the systems are documented in Hsu *et al* (2017), Reddin *et al* (2018), Zhang *et al* (2018), Rausch *et al* (2019), and van Sluis *et al* (2019). The geometric configurations of the three PET systems were modelled in GATE, incorporating dimensions and material compositions as specified by the manufacturers.

The design was based on a cylindrical geometry, with components organised into four hierarchical levels: *Sectors*, *Blocks*, *Mini-Blocks* and *Crystals* (figure 1). The arrangement and materials of the detector blocks and mini-blocks, the internal structure of the plastic housing surrounding the field of view (FOV), and the patient bed were also modelled (Salvadori *et al* 2020). This step is important to account for scatter radiation and attenuation effects in surrounding materials.

2.2. NEMA count losses and scatter fraction

Experimental evaluations were conducted in accordance with the NEMA count losses protocol (NEMA 2018), following the manufacturer's acquisition guidelines. An ^{18}F line source, with a radius of 1.6 mm and a length of 700 mm, was placed within the NEMA scatter phantom—a solid polypropylene cylinder with a radius of 102 mm and a length of 700 mm. The source, initially filled to achieve the peak value of noise equivalent count rate (NECR) for each PET system, contained activities of 1616 MBq for the Vereos, 1210 MBq for the Vision, and 718 MBq for the DMI 4-ring.

The scatter phantom was placed on the patient bed and centred in the FOV, with the line source offset by 45 mm from the cylinder's central axis. Several acquisitions were performed over a period of 16 hours, following the manufacturer's protocol. Total, random, true, scatter and NEC rates (Tot, R, T, S and NECR) were determined for each acquisition frame according to the NEMA standard (NEMA 2018).

Both the Vereos and Vision PET systems estimate random coincidences from the measured delayed coincidences, with noise regularisation through variance reduction. On the other hand, the DMI 4-ring

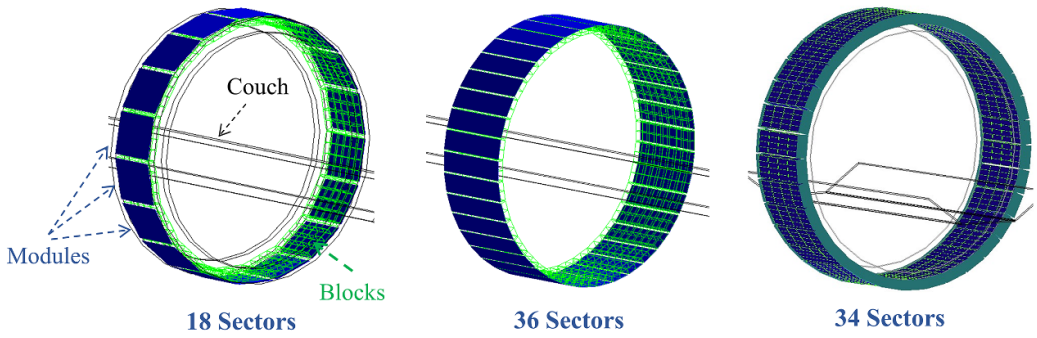

	VEREOS	VISION 600	DMI 4-ring
LEVEL 1: SECTORS	131.4 x 164 mm² = 4 x 5 Blocks	64.6 x 264.8 mm² = 2 x 8 Blocks	64.5 x 199.7 mm² = 1 x 4 Blocks
LEVEL 2: BLOCKS	32.6 x 32.6 mm² = 4 x 4 Mini-blocks	32.2 x 32.2 mm² = 2 x 2 Mini-blocks	64.5 x 47.8 mm² = 4 x 1 Mini-blocks
LEVEL 3: MINI-BLOCKS	8 x 8 mm² = 2 x 2 LYSO **Crystals**	16 x 16 mm² = 5 x 5 LSO **Crystals**	15.8 x 47.7 mm² = 4 x 9 LYSO **Crystals**
LEVEL 4: CRYSTALS	**LYSO Crystal** (4 x 4 x 19 mm³)	**LSO Crystal** (3.2 x 3.2 x 20 mm³)	**LYSO Crystal** (5.3 x 3.95 x 25 mm³)

Figure 1. GATE geometric models of the Vereos, Vision 600, and DMI 4-ring PET systems, all featuring 4 depth levels. The Vereos system includes 18 *Sectors*, while the Vision 600 and DMI 4-ring comprise 36 and 34 *Sectors*, respectively. Within the detection system, the total number of crystals is 23 040 for Vereos, 38 912 for Vision 600, and 19 584 for DMI 4-ring.

system estimates randoms based on single event counts. In both cases (delayed and single method), the estimation of randoms was considered noise-free, and the NECR was calculated without additional noise contributions using the formula, NECR $= \frac{T^2}{T+S+R}$.

2.3. Experimental determination of background noise

The data frames from the NEMA count losses assessment were analysed to investigate the relationship between the single event rate of a *Sector* and the activity concentration. The single event rate for a *Sector* was derived from the system-wide single event rate, assuming uniform single event rates and detection efficiencies across all detectors.

The experimental background noise was assessed using linear regression on the single event rates measured at low activity concentrations (below 3 kBq·ml^{-1}). This regression (S_{nDT}), extrapolated to zero activity, provided the single event rate in the absence of any activity in the FOV, denoted λ_{exp}. This rate, derived from the experimental single event rates, reflects the background noise at the end of the detection process, accounting for detection efficiency and energy thresholding.

2.4. Generic digitizer model

In GATE, the interactions of a particle in the crystals are called *hits* (Sarrut *et al* 2021). Along the detection chain, the *hits* are grouped, converted into *singles*, and sorted into *coincidences* by the digitizer. The digitizer is a signal processing chain composed of a sequence of modules, each associated with specific parameters. To faithfully replicate the count rates observed in actual PET systems, both the model and the associated parameters require precise tuning. As shown in figure 2, the generic digitizer model encompasses nine sequential modules: (1) Adder, (2) Readout, (3) Background noise, (4) Detection efficiency, (5) Energy blurring, (6) Temporal resolution, (7) Pile-up, (8) Energy thresholds, and (9) Coincidence sorter. The parameters of these nine modules are detailed in table 3. When possible, parameters were set based on specifications provided by the manufacturers. Otherwise, parameters were estimated through an optimisation process and validated against experimental data. These parameters are described in detail in the following subsections.

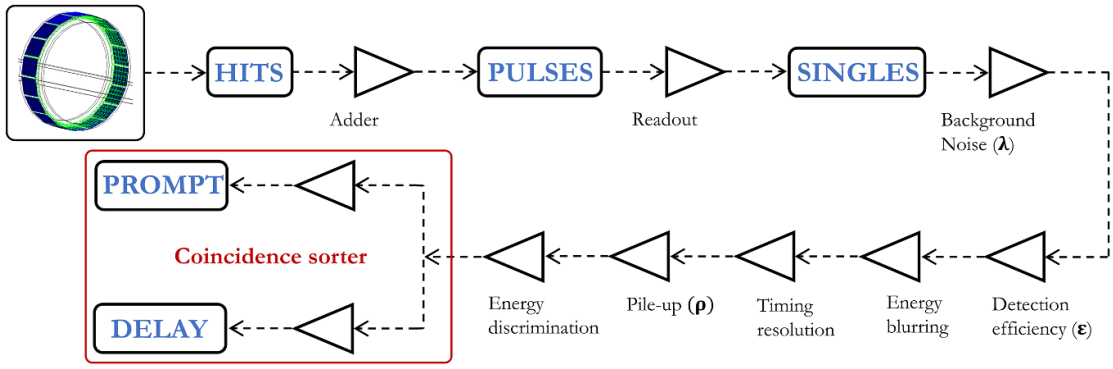

Figure 2. The proposed generic digitizer model, illustrating the three key parameters remaining for optimisation: the background event rate (λ), the detection efficiency correction factor (ϵ), and the pile-up integration time for single events (ρ).

2.4.1. Adder and readout

The *Adder* constitutes the initial module in the digitization chain. For each primary event, it groups the *hits* occurring in a given detection volume into *pulses*. This is done by first summing the energy deposited by all the hits and then calculating the energy-weighted centroid position.

The *Readout* module groups and computes the output position of the combined hits at a given geometrical level of the system, generating what are referred to as *singles*. This module incorporates two strategies for signal integration based on energy: the *winner-takes-all* policy, simulating 1:1 coupling between crystals and SiPM detectors—as done in Salvadori *et al* (2020) - and the *energy centroid* policy, simulating the multiplexed readout (Anger's logic) - as done in Merlet *et al* (2024)). In the first case, the *winner-takes-all* approach allows for user-defined readout levels, identifying the interacting crystal as the one with the highest energy deposition. In the second case (*energy centroid*), signal integration occurs one geometrical level above the crystal level (see figure 1), with the position of interaction determined by the energy-weighted centroid of hits within that volume. All three evaluated PETs have a SiPM-based detection system. Although Vereos uniquely features a true 1:1 SiPMs coupling, the *winner-takes-all* approach was preferred, as it accurately reflects the SiPMs readout structure and offers enhanced flexibility with respect to the readout level.

In actual systems, signal integration occurs (1) at the block level (level 2) for the Vision, providing a readout area of $32\times$ 32 mm^2 (Reddin *et al* 2018), and (2) at the mini-block level (level 3) for both the Vereos and the DMI 4-ring, with readout areas of 8×8 mm^2 (Schaart *et al* 2016) and 16×48 mm^2 (Wagadarikar *et al* 2014), respectively. Since GATE currently lacks a module in the digitizer for modelling the scattered photon recovery process (Wagadarikar *et al* 2014), signal integration for all systems was executed at level 1 (*Sectors*) to mitigate potential underestimation of sensitivity (Salvadori *et al* 2020) (see discussion).

2.4.2. Background noise and detection efficiency

Background noise (BN) represents the rate of single events detected by the system when there is no activity in the FOV. This noise may originate from detection electronics, dark counts inherent to SiPM-based detection systems (Gundacker and Heering 2020), or the natural radioactivity of the scintillation crystals (^{176}Lu for LYSO and LSO). Positioned at the beginning of the detection chain, before the detection efficiency module, BN aims to replicate the noise contribution at the end of the digitization chain (after energy selection). Consequently, the *energy* distribution of background events is modelled by a Gaussian centred at 511 keV with a standard deviation of 1 keV, ensuring that the entire distribution falls within the energy window. The *time* distribution of background events is assumed to follow a Poisson distribution, with the probability of detecting n background events in a time interval t given by $P(n,t) = \frac{(\lambda t)^n}{n!}e^{-\lambda t}$, where λ is the average background event rate.

The detection efficiency (DE) module compensates for detection losses not accounted for in the simulation and corrects for any inaccuracies in geometry and material composition, with ϵ representing the fraction of *singles* accepted by the module. Since ϵ and λ are modelled at the beginning of the detection chain, before energy windowing, direct measurement in clinical systems is impractical. Thus, an optimisation method for these parameters, coupled with indirect experimental validation, is proposed in section 2.5.1.

2.4.3. Energy and timing resolutions

The coincidence timing resolution (CTR) and energy resolution (ER) at 511 keV for the Vereos, Vision, and DMI 4-ring are documented to be 310 ps, 11.2% (Rausch *et al* 2019), 210 ps, 9.0% (Reddin *et al* 2018), and 374 ps, 9.4% (Hsu *et al* 2017), respectively. In GATE, these parameters are implemented through Gaussian

convolutions applied to the timestamps and energies of the *singles*, with the timing resolution module parameterised by the single timing resolution (STR), defined as $\text{STR} = \frac{\text{CTR}}{\sqrt{2}}$.

2.4.4. Dead time and pile-up

Dead time represents the duration τ after each event, during which the system cannot detect another event. Pile-up effect is the potential detection of multiple events during the signal integration time ρ. These two deleterious effects are responsible for the saturation of the system when the incoming photon rate increases. Modelling of both effects is important at high activity. Following the readout module, dead time and pile-up were applied at the *sectors* level (level 1).

Dead time can be modelled either before or after the energy window, without affecting the scatter fraction. If modelled after the energy window, experimentally determined dead time values can be used. Alternatively, if modelled before the energy window, an optimisation process is required. Unlike dead time, pile-up is directly related to energy thresholding, as stacking two single events can either move a true coincidence photon's signal outside the energy window or occasionally move a scattered photon's signal inside the energy window, thus affecting the scatter fraction.

Therefore, both pile-up and dead time were modelled before energy discrimination, following an optimisation process. Initially, the pile-up integration time was optimised to match the experimental scatter fraction, followed by dead time optimisation to match the experimental single event rates. However, for all PET systems, optimal scatter fractions were achieved without underestimating the single rates when dead time was set to 0. Consequently, dead time was removed from the digitizer chain.

2.4.5. Energy windows

The energy window widths were set to 449.7–613.2 keV for the Vereos, 435–585 keV for the Vision, and 425–650 keV for the DMI 4-ring, in accordance with the manufacturers' specifications. The minimum transverse *Sector* difference (*minSectorDifference*) required to define a valid line-of-response was also set in accordance with the manufacturers' recommendations: five for the Vereos (80°), five for the Vision (44.5°), and four for the DMI 4-ring (42.4°).

2.4.6. Coincidence sorter

According to the manufacturers' specifications, *single* events were paired by the coincidence sorter module (Strydhorst and Buvat 2016) using a time coincidence window (TCW) of width 2.0115 ns (Vereos), 2.3633 ns (Vision) and 2.4543 ns (DMI 4-ring).

GATE offers two methodologies for the *allDigiOpenCoincGate* policy, used to aggregate single events into coincidences. The first, known as *single-window*, initiates a TCW upon detecting a single event, during which no additional TCWs can be opened by other single events. The alternative, known as *multiple-window*, allows each single event to trigger its own TCW, with a logical OR operation applied to all windows to identify coincidences. Based on Salvadori *et al* (2020), Kalaitzidis *et al* (2022), and Merlet *et al* (2024), the *multiple-window* approach was used as it offers a better modelling of clinical PET count rates.

Given the width of the TCW, a particular single event may fit to be paired with multiple other single events. GATE provides nine policies to deal with these multiple coincidences. As described by Moraes *et al* (2015), the coincidence policy currently implemented in modern PET systems is best modelled by the *takeAllGoods* policy. In this case, all multiple coincidences are accepted: i.e. a single event detected at time t defines a coincidence with all single events detected between t-TW and t+TW. The combination of the *multiple-window* and *takeAllGoods* policies has been shown to better estimate random coincidences when using the delayed time window method (Strydhorst and Buvat 2016). In addition, this combination was the only one that allowed our models to generate a sufficient number of coincidences to accurately replicate the observed experimental prompt rates.

Philips (Vereos) and Siemens (Vision 600) use the delayed coincidence window technique to estimate the distribution of random coincidences (Brasse *et al* 2005). According to the manufacturers' specifications, an additional coincidence window of identical width has been incorporated for these systems, with a delay of 100 ns for the Vereos and 13 ns for the Vision. Conversely, GE derives random coincidence estimates directly from single event counts (Stearns *et al* 2003), and therefore does not use delayed windows. In this method, the random coincidence rate r_{xy} between two detectors x and y, with their respective single event rates s_x and s_y, is calculated as $r_{xy} = 2\,\text{TCW}\,s_x\,s_y$.

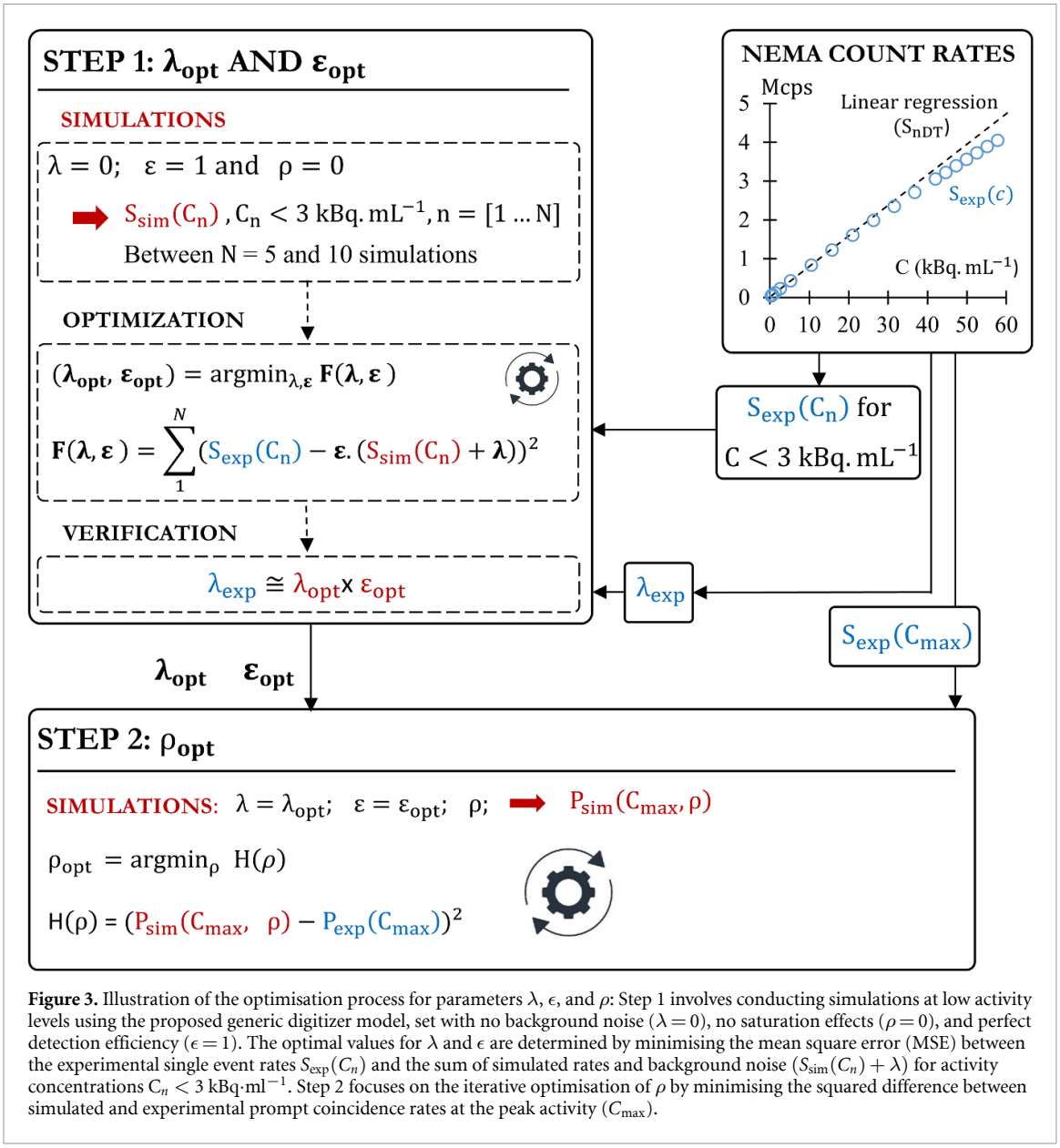

Figure 3. Illustration of the optimisation process for parameters λ, ϵ, and ρ: Step 1 involves conducting simulations at low activity levels using the proposed generic digitizer model, set with no background noise ($\lambda = 0$), no saturation effects ($\rho = 0$), and perfect detection efficiency ($\epsilon = 1$). The optimal values for λ and ϵ are determined by minimising the mean square error (MSE) between the experimental single event rates $S_{exp}(C_n)$ and the sum of simulated rates and background noise ($S_{sim}(C_n) + \lambda$) for activity concentrations $C_n < 3$ kBq·ml^{-1}. Step 2 focuses on the iterative optimisation of ρ by minimising the squared difference between simulated and experimental prompt coincidence rates at the peak activity (C_{max}).

2.5. Optimisation of the digitizer chain

The previous section detailed the main components of the digitizer as depicted in figure 2, setting several parameters such as readout (using the *winner-takes-all* policy at level (1), energy and timing resolutions and windows (as per specifications), and the process for coincidence sorting (using the *multiple-window* and *takeAllGoods* approaches). However, three parameters remain undetermined: the average background event rate (λ), the detection efficiency correction factor (ϵ) and the pile-up integration time for single events (ρ) as introduced in section 2.4. The determination of these parameters involved two optimisation processes.

First, λ and ϵ were optimised by fitting the simulated single event rates with experimental data at low activity levels. The second optimisation considered pile-up modelling and optimises ρ to fit prompt event rates at high activity. This two-steps optimisation is detailed in the following subsections and illustrated in figure 3.

2.5.1. Step 1 - background noise and detection efficiency

At this stage, the detection efficiency factor ϵ remains undefined. Furthermore, the experimentally measured background noise (λ_{exp}) cannot be used directly, as it reflects the noise level *after* the unknown DE factor. Therefore, λ_{opt} and ϵ_{opt} were derived by adjusting the simulated single event rate against experimental data at low activity levels. This calibration involved running N simulations (ranging from 5 to 10, according to the

PET system) under low activity conditions $C_n < 3$ kBq·ml^{-1} for $n = N$, employing a digitizer configured with $\lambda = 0$, $\epsilon = 1$, and $\rho = 0$—modelling a system with no background noise, no saturation effects, and perfect detection efficiency. Each simulation was conducted with 1 million prompts (Salvadori *et al* 2020). Subsequently, λ and ϵ were optimised using equations (1) and (2), with least-square optimiser

$$\left(\lambda_{\text{opt}}, \epsilon_{\text{opt}}\right) = \arg\min_{\lambda,\epsilon} F(\lambda, \epsilon) \tag{1}$$

$$F(\lambda, \epsilon) = \sum_{n=1}^{N} \left(S_{\text{exp}}\left(C_n\right) - \epsilon\left(S_{\text{sim}}\left(C_n\right) + \lambda\right)\right)^2. \tag{2}$$

Given that BN precedes DE in the model, the product $\lambda_{\text{opt}} \times \epsilon_{\text{opt}}$ was compared with the experimental background noise (λ_{exp}) to validate the accuracy of the optimisation.

2.5.2. Step 2 - PILE-up

The pile-up integration time ρ was optimised by minimising the squared difference between the simulated and experimental prompt coincidence rates. A grid search was performed using simulations with several ρ values, at the peak activity frame C_{max}, with $\lambda = \lambda_{\text{opt}}$ and $\epsilon = \epsilon_{\text{opt}}$. The grid search was stopped once the relative difference $\sqrt{H}/P_{\text{exp}}(C_{\text{max}})$ was lower than 0.02

$$\rho_{\text{opt}} = \arg\min_{\rho} H(\rho) \tag{3}$$

$$H(\rho) = \left(P_{\text{sim}}\left(C_{\text{max}}, \rho\right) - P_{\text{exp}}\left(C_{\text{max}}\right)\right)^2. \tag{4}$$

2.6. Validation of the digitizer model

After optimisation, the performance of the digitizer was assessed following the NEMA count loss protocol as outlined in section 2.2. Proprietary scripts, validated by comparing experimental results with those from the manufacturer's software, were developed for each PET system to enable analysis of both experimental and simulated data using the same code. Data for the Vereos and Vision 600 were recorded and simulated in list mode (LM) and analysed using LM-based methods. Conversely, for the DMI 4-ring, data were recorded, simulated, and analysed using a sinogram-based approach. For all systems, multiple Monte Carlo simulations were conducted, each mirroring an experimental NECR frame with 2 million prompts per simulation. The simulated and experimental measurements of prompt, random, true, scatter, and NECR rates were compared, focusing on relative discrepancies.

3. Results

3.1. Experimental determination of background noise and dead time

Figure 4(A) presents the correlation between the rate of detected singles and the activity concentration, as derived from the NEMA count rate test. The linear regression for low activity levels (< 3 kBq·ml^{-1}) is also shown. Table 1 lists the linear regression coefficients and quality metrics, along with the experimental background rate (λ_{exp}). For each regression, the coefficient of determination R^2 and the root mean square error (RMSE) are included. The parameter 'b' of the linear fit is scaled by the number of *Sectors* N_{sector} to obtain λ_{exp}, the overall experimental background event rate for the system.

Figure 4(B) shows that the Vereos system has the lowest count loss with increasing activity levels. At an activity concentration of 23.5 kBq·ml^{-1}, corresponding to the peak NECR for the DMI 4-ring, the dead time factor ($\frac{S_{\text{nDT}}}{S_{\text{exp}}}$) was 1.05, 1.15, 1.09 for the Vereos, Vision 600 and DMI 4-ring, respectively. Notably, the DMI 4-ring's detection system encounters a significantly higher background event fluence rate (BN per unit area) compared to the Vision 600 or Vereos, with values of 2.664, 1.067, and 1.022 cps.mm^{-2}, respectively.

3.2. Optimisation of the digitizer chain

For background noise and detection efficiency, table 2 shows the results of the optimisation of λ and ϵ. Relative differences between $\lambda_{\text{opt}} \times \epsilon_{\text{opt}}$ and λ_{exp} were below 0.5%. The optimised pile-up integration times (ρ_{opt}) were 5.6 ns, 19.2 ns and 20 ns for the Vereos, Vision 600 and DMI 4-ring, respectively.

To illustrate the usefulness of each step in the proposed method, figure 5 presents the results for the Vision 600, including prompt, delay, scatter, true, NEC rates, and scatter fraction, both without optimisation

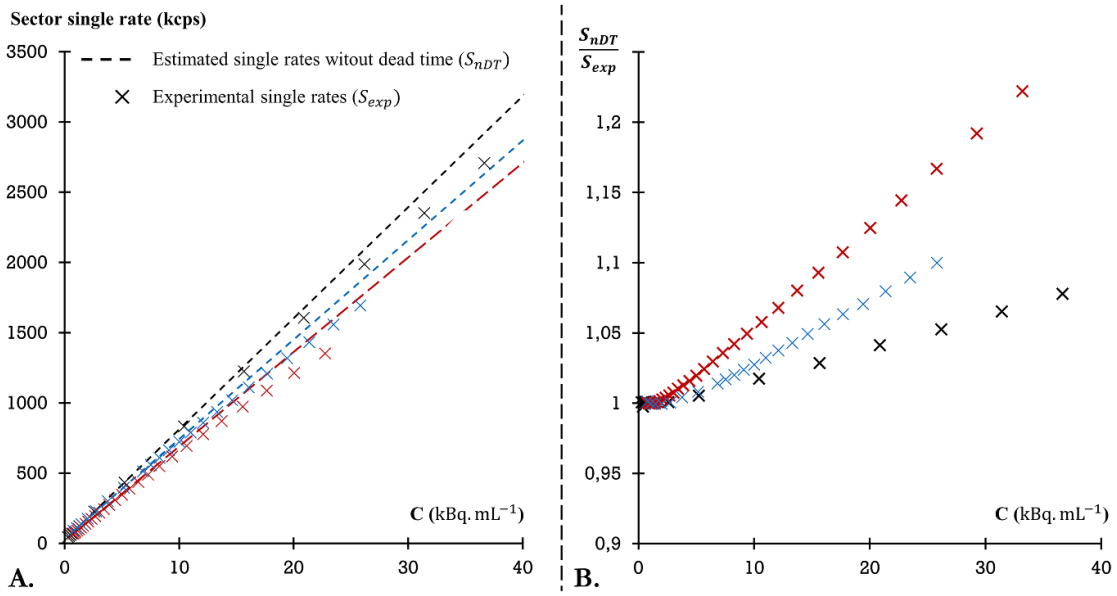

Figure 4. (A) Relationship between single count rates at the *Sector* level (S_{exp}, represented by cross symbols) and activity concentration derived from the NEMA count losses test for the Vereos (black), Vision (red), and DMI 4-ring (blue) PET systems. The linear regressions at low activity levels (< 3 kBq·ml^{-1}) are shown (dashed lines), predicting single count rates without dead time (S_{nDT}). (B) The dead time factor ($\frac{S_{nDT}}{S_{exp}}$) as a function of activity concentration.

Table 1. Parameters of the linear regression used to model the single rate at the *Sector* level without dead time (a and b) with associated goodness of fit criteria (R^2 and RMSE). The parameter 'b' is scaled by the number of *Sectors* N_{sector} to obtain λ_{exp}, the overall experimental background event rate.

	Linear regression parameters $S_{nDT} = a \times C + b$		Goodness of fit		Background noise
	a	b	R^2	RMSE	$\lambda_{exp} = b \times N_{sector}$
Vereos	79.07	22.03 kcps	> 0.99	0.07	396.58 kcps
Vision 600	67.31	17.30 kcps	> 0.99	0.02	657.19 kcps
DMI 4-ring	70.83	34.32 kcps	> 0.99	0.09	1166.71 kcps

Table 2. Optimised values of λ and ϵ. $\lambda_{opt} \times \epsilon_{opt}$ is compared to λ_{exp}.

	λ_{opt} (kcps)	ϵ_{opt}	$\lambda_{opt} \times \epsilon_{opt}$ (kcps)	λ_{exp} (kcps)	Δ (%)
Vereos	461.0	0.861	397.03	396.58	0.1
Vision 600	710.0	0.927	658.31	657.19	0.2
DMI 4-ring	1198.0	0.977	1170.19	1166.71	0.3

and after each optimisation step. Optimising detection efficiency (ϵ) and background noise (λ) enables precise modelling at low activity levels. Detection efficiency impacts all count rates, while background noise predominantly affects random rates (figure 5(B)). Additionally, modelling of pile-up integration time (ρ) compensates for count losses and captures the overall trend of the scatter fraction, despite an observed offset. Corresponding figures for the Vereos and the DMI 4-ring are available in the supplementary files A1 and B1.

3.3. Validation of the digitizer model

As shown in figure 6, the simulations exhibit excellent agreement with the experimental data for prompt coincidence rates for all three systems, with the maximum relative discrepancy not exceeding 3% over the entire range of activity concentrations. The agreement for random coincidence rates was also commendable, showing a maximum relative difference of less than 7%. The maximal relative deviations observed for prompt, random, true, and scatter coincidences were (2.5%, −3.0%, 6.7%, −14.5%), (−1.6%, −3.1%, 2.8%, −8.3%), and (−1.9%, −6.2%, 11.6%, −6.4%) for the Vereos, Vision 600, and DMI 4-ring, respectively.

With increasing activity concentration, there was a noticeable trend toward progressive overestimation of the simulated true event rates and NECR, particularly for the DMI 4-ring. The relative difference for the DMI 4-ring escalated from 3.0% (true) and 7.5% (NECR) at 5 kBq·ml^{-1} to 11.6% and 24.6% at the activity level of the NECR peak (23.47 kBq·ml^{-1}). Similarly, a progressive underestimation of simulated scatter event

Table 3. Parameter values for the final configuration of the digitizer. The parameters in blue are those that have been optimised.

PET system	Vereos	Vision 600	DMI 4-ring
	Singles		
Readout level	1	1	1
Readout policy	winner-takes-all	winner-takes-all	winner-takes-all
Background noise energy distribution	Gauss, FWHM 1 keV	Gauss, FWHM 1 keV	Gauss, FWHM 1 keV
Background noise time distribution	Poisson λ_{opt} = 461 kcps	Poisson λ_{opt} = 710 kcps	Poisson λ_{opt} = 1198 kcps
Energy blurring	11.2%	9%	9.4%
Detection efficiency	ϵ_{opt} = 0.861	ϵ_{opt} = 0.927	ϵ_{opt} = 0.977
Singles timing resolution	220 ps	178.5 ps	265.9 ps
Pile-up level	1	1	1
Pile-up value	ρ_{opt} = 5.6 ns	ρ_{opt} = 19.2 ns	ρ_{opt} = 20 ns
Energy window	449.7–613.2 keV	435–585 keV	425–650 keV
	Coincidences		
Sorter type	Multiple-window	Multiple-window	Multiple-window
Time coincidence window	2.0115 ns	2.3633 ns	2.4543 ns
MultiplePolicy	takeAllGoods	takeAllGoods	takeAllGoods
Delay offset	100 ns	13 ns	NA
MinSectorDifference	5	5	4

rates was observed for the Vereos and Vision 600 systems, with the relative difference increasing from −5.3% (Vereos) and −6.2% (Vision 600) at 5 kBq·ml^{-1} to −14.5% and −8.3% at the activity level of the NECR peak (57.59 kBq·ml^{-1} and 29.25 kBq·ml^{-1}). The overestimation of the simulated true event rate and the underestimation of the simulated scatter event rate, when compared to experimental data, lead to a consistent underestimation of the simulated scatter fraction for all three systems. At the activity concentration corresponding to the NECR peak, the relative deviation was −14.1%, −6.1%, and −5.8% for the Vereos, Vision 600, and DMI 4-ring, respectively.

For all systems evaluated, the activity at the NECR peak, denoted C_{peak}, closely matched experimental values, with discrepancies of less than 5%. Nevertheless, the simulated true coincidences' overestimation led to an overestimated $NECR_{peak}$ by 14.4% and 24.6% for the Vereos and DMI 4-ring, respectively. $NECR_{peak}$ and associated C_{peak} values are summarised in table 4.

As detailed in table 5, the maximum relative differences between all simulated event rates and experimental data remained within 12% for activity concentrations in the range of 0–10 kBq·ml^{-1}, reflecting the clinical rates typically observed in whole-body ^{18}F scans (Salvadori *et al* 2021). This maximum disparity extended to 20.8% (NECR for the DMI 4-ring) for activity concentrations ranging up to 21 kBq·ml^{-1}, as encountered in ^{82}Rb cardiac examinations (Salvadori *et al* 2021).

4. Discussion and conclusion

This work presented a versatile methodology for modelling and optimising PET digitizers within GATE. It was applied to three state-of-the-art SiPM-based TOF-PET systems and validated by comparison with experimental data. The simulated prompt rates demonstrated remarkable consistency with the experimental prompt rates, with relative differences below 2.5% across all systems and activity ranges. The modelling of random coincidences was also satisfactory, with maximum discrepancies not exceeding 7%.

However, as activity concentrations increased, a noticeable pattern emerged where simulated true rates were overestimated and simulated scatter rates were underestimated. This overestimation of true rates has a quadratic effect on the NECR, while the divergent trends between true and scatter rates result in a systematic underestimation of the scatter fraction throughout the activity spectrum. This discrepancy has not been fully elucidated but may stem from the GATE model, incorporating variations in the geometric modelling or material composition of the phantoms and detection systems, as well as a potential oversimplification in modelling saturation effects (pile-up and dead time) in the digitizer. Furthermore, uncertainties in the experimental acquisition could also be contributory, such as the uniform activity distribution in the line source. For instance, discrepancies in $NECR_{peak}$ values of the DMI 4-ring have been noted: 180 kcps according to GE specifications (GE Healthcare 2016), 164 kcps in this study, and 200 kcps reported by Hsu *et al* (2017). Consequently, variations in the experimental $NECR_{peak}$ value could lead to differences in the optimisation of digitizer values. Finally, conducting signal integration at the highest level (*Rsector*) due to the lack of a scatter recovery implementation in GATE might have contributed to these discrepancies. This allows

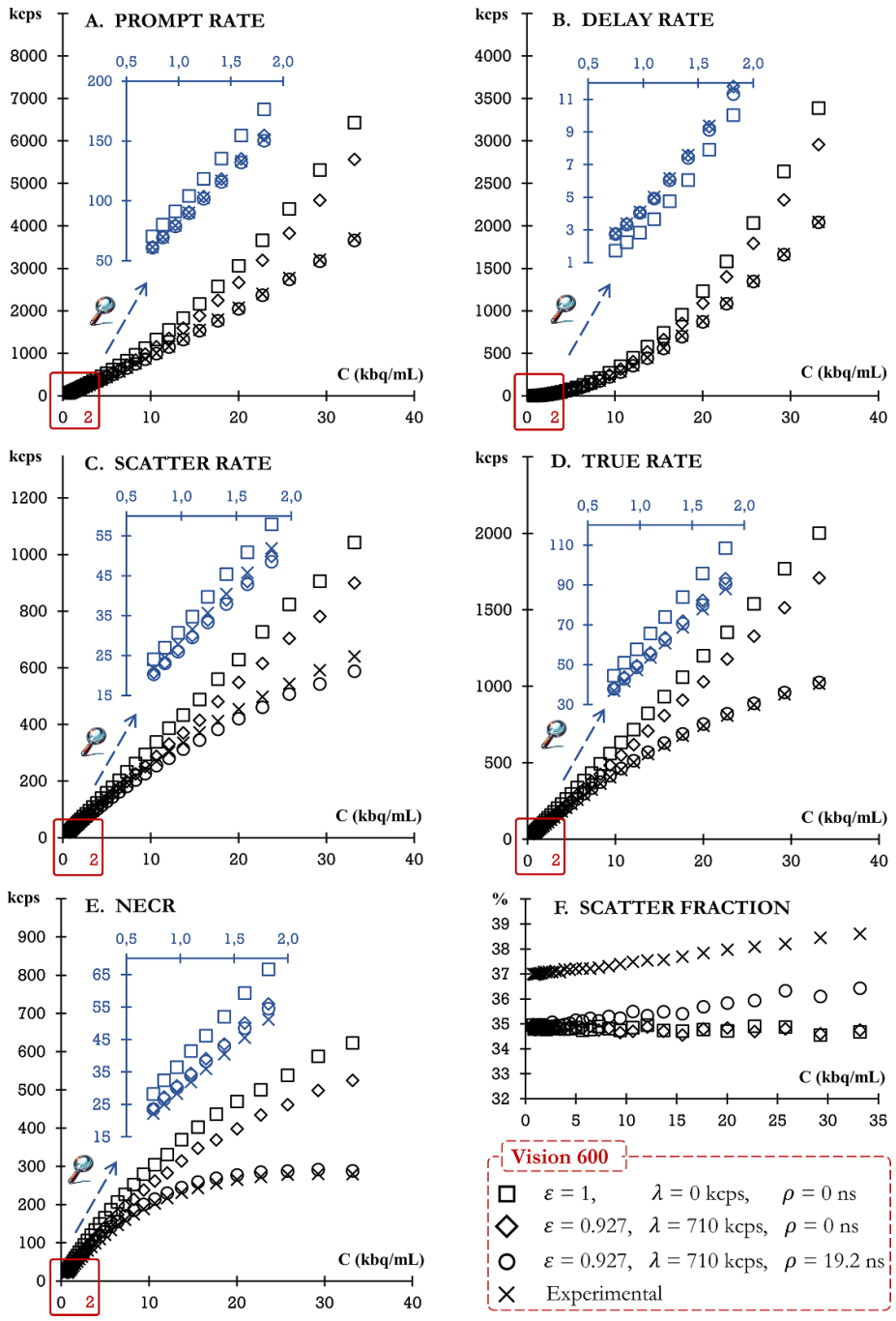

Figure 5. Simulated prompt, delay, scatter, true, NEC rates, and scatter fraction for the Vision system without optimisation ($\epsilon = 1$, $\lambda = 0$ kcps, $\rho = 0$ ns; square symbols), followed by each optimisation step: (1) optimisation of background noise and detection efficiency ($\epsilon = 0.927$, $\lambda = 710$ kcps, $\rho = 0$ ns; diamond symbols), and (2) integration time adjustment for pile-up effects ($\epsilon = 0.927$, $\lambda = 710$ kcps, $\rho = 19.2$ ns; circle symbols). Cross symbols represent experimental data.

the model to reach the experimental sensitivity, but may also influence the scatter fraction. Nevertheless, the proposed method reproduces the experimental count rates in all systems, with relative inaccuracies of less than 12% for clinically relevant ^{18}F activity concentrations (0-10 kBq·ml^{-1}) and less than 21% for higher activities up to 21 kBq·ml^{-1} seen in ^{82}Rb cardiac studies.

The GATE Dead-Time module for single events was not included in the digitizer chain, as discussed in section 2.4.4. This decision highlights the potential oversimplifications in the representation of saturation effects within the GATE digitizer framework. Such simplifications might contribute to the observed challenges in accurately aligning the scatter fractions and single/prompt event rates at high activity levels (figure 5). Improvements to the digitizer are anticipated in the forthcoming GATE version 10 (Sarrut *et al* 2022).

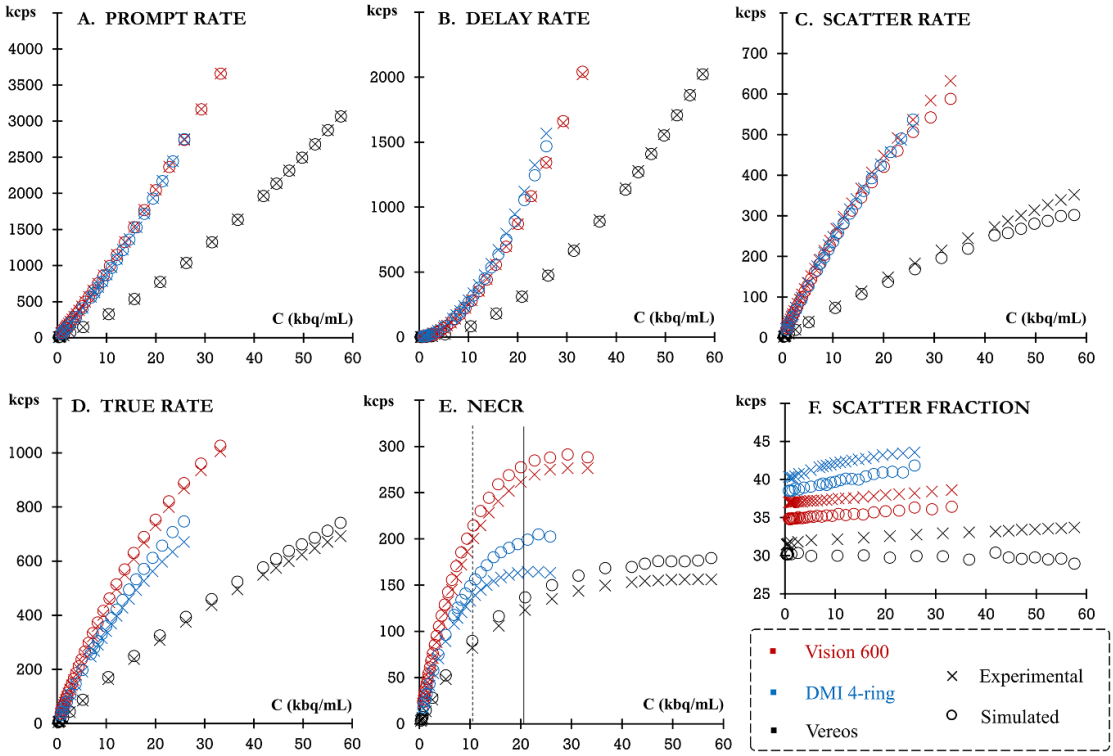

Figure 6. Comparison of simulated and experimental data for prompt, delayed, scattered, true, and NEC rates up to the peak NECR activity level. Vertical lines indicate the peak activity concentrations typically encountered in clinical PET examinations, with ^{18}F (dashed line) and ^{82}Rb (solid line) denoting the specific isotopes used.

The Vereos system showed lower count losses as activity levels increased, in comparison to the other two systems, as depicted in figure 4. Specifically, at an activity level of 23.47 kBq·ml^{-1}, which corresponds to the peak activity (A_{peak}) of the DMI 4-ring, the count loss for the Vereos is significantly lower than that for the Vision 600 and DMI 4-ring, with dead time factors being 9.9% and 4.1% lower, respectively. This reduction in count losses at higher activity concentrations can be attributed to the increasing impact of dead time and pile-up effects, both of which are inversely related to the size of the trigger domains, i.e. the detection surface area associated with each trigger circuit. The Vereos uses considerably smaller trigger domains compared to the Vision 600 and DMI 4-ring (0.64 cm^2 versus 10.37 cm^2 and 7.68 cm^2, respectively), leading to a substantial decrease in the data flow per trigger circuit, which in turn, effectively mitigates the dead time and pile-up effects (Salvadori *et al* 2021).

The DMI 4-ring detection system exhibited the highest background event fluence rate (BN per unit area), which was 161% and 150% higher than the Vision 600 and Vereos systems, respectively (2.66 vs 1.07 and 1.02 cps.mm^{-2}). This may be due to its wider energy window (225 keV vs 150 keV for Vision 600 and 164 keV for Vereos) and thicker crystals (25 mm vs 20 mm for the Vision 600 and 19 mm for the Vereos). Intriguingly, despite having a 7.3% wider energy window and similar crystal length compared to the Vision 600 (164 keV vs 150 keV and 19 mm vs 20 mm, respectively), the Vereos system showed a marginally lower background fluence rate than the Vision 600 (1.022 vs 1.067 counts s^{-1} mm^{-2}). This discrepancy could be attributed to an interesting feature of the digital SiPM technology used in the Vereos, which, unlike the analog SiPM-based detection systems of the DMI 4-ring and Vision 600 where Geiger-mode avalanche photodiodes (G-APDs) are connected in parallel, allows for the digital detection and counting of individual G-APD breakdowns. Each G-APD in the digital SiPM system has a memory bit, allowing the diode to be turned on or off. It could be used to deactivate diodes exhibiting high dark counts, potentially reducing background noise (Frach *et al* 2009, Gundacker and Heering 2020).

This study presented an innovative methodology to develop and validate a generic digitizer model within GATE for various state-of-the-art PET systems. A distinctive aspect of this approach lies in the accurate emulation of the geometries and digitizer chains with a minimal number of parameters to be optimised. The optimisation is confined to single and prompt event rates, with an expectation that this would lead to congruence among all count rates.

This work could be useful to better understand the behaviour of PET systems and to support the development of new PET designs.

Table 4. Peak NECR values ($NECR_{peak}$) and associated activity concentrations (C_{peak}).

	C_{peak} (kBq·ml^{-1})			$NECR_{peak}$ (kcps)		
	Vereos	Vision 600	DMI 4-ring	Vereos	Vision 600	DMI 4-ring
Simulated	57.59	29.25	23.47	179356	291375	204923
Experimental	54.98	29.25	23.47	156854	279964	164447
Relative difference	4.76%	0.00%	0.00%	14.35%	4.08%	24.61%

Table 5. Maximum relative difference between simulated (study) and experimental (reference) data across all acquisitions. Values are reported for two activity ranges: clinical ^{18}F scans and ^{89}Rb cardiac perfusion scans.

	^{18}F [0-10 kBq·ml^{-1}]			^{82}Rb [0-21 kBq·ml^{-1}]		
	Vereos	Vision 600	DMI 4-ring	Vereos	Vision 600	DMI 4-ring
Prompt	2.5%	−1.4%	−1.9%	2.5%	−1.6%	−1.9%
Random	−3.0%	−3.1%	−5.3%	−3.0%	−3.1%	−5.9%
True	4.3%	2.8%	5.2%	4.9%	2.8%	9.7%
Scatter	−5.9%	−6.8%	−6.4%	−7.9%	−7.4%	−6.4%
NECR	8.5%	6.6%	11.8%	10.7%	6.6%	20.8%

Data availability statement

GATE scripts for simulation during the current study are available from the corresponding author upon reasonable request.

All data that support the findings of this study are included within the article (and any supplementary information files).

Acknowledgments

This work was carried out within the framework of the MOCAMED project (ANR-20-CE45-0025), the SIRIC LYriCAN Grant INCa-DGOS-INSERM-ITMO cancer_18003, the LABEX PRIMES (ANR-11-LABX-0063) of Université de Lyon, within the program 'Investissements d'Avenir' (ANR-11-IDEX-0007).

Appendix A. Vereos digitizer optimisation

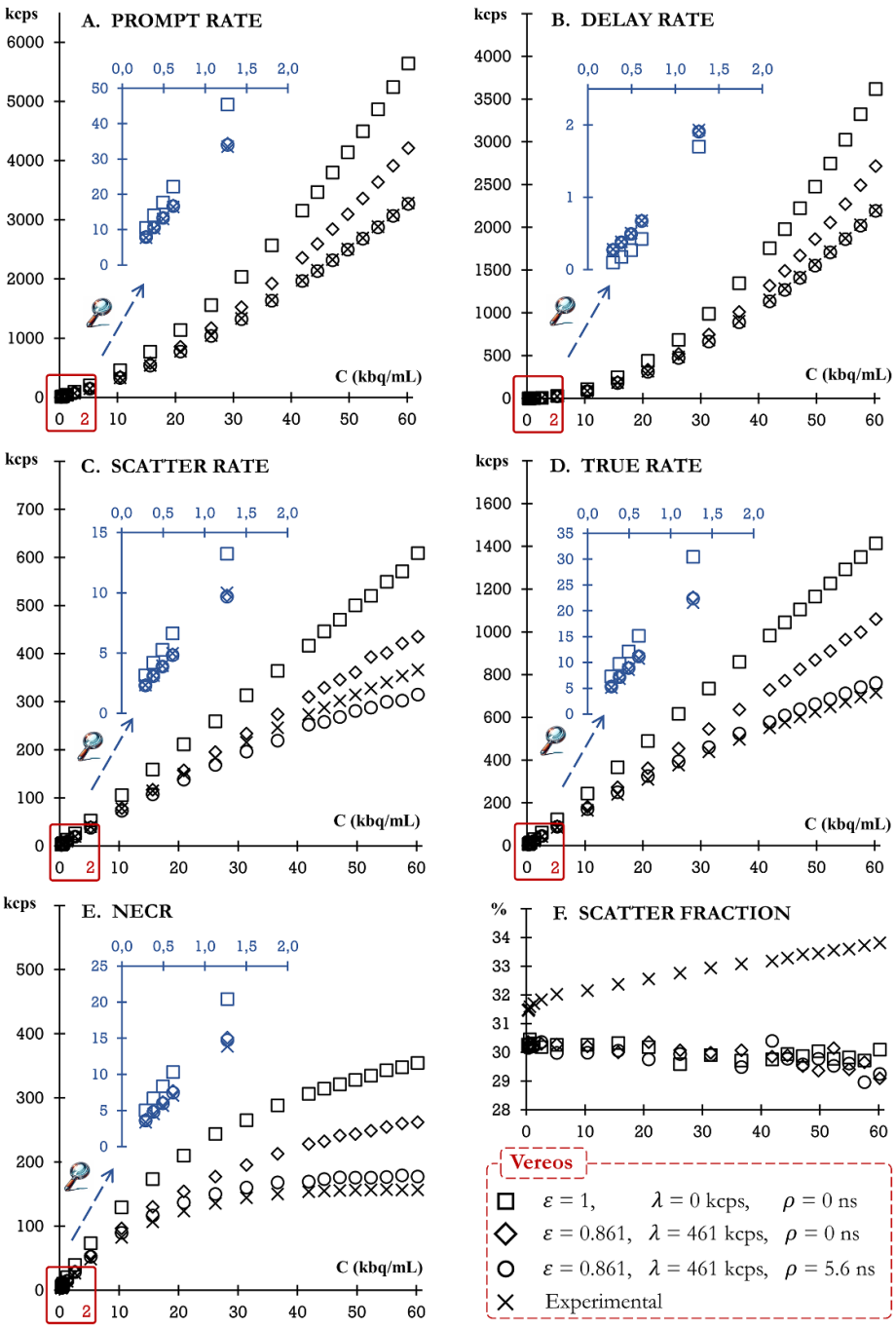

Figure A1. Simulated prompt, delay, scatter, true, NEC rates, and scatter fraction for the Vereos system without optimisation ($\epsilon = 1$, $\lambda = 0$ kcps, $\rho = 0$ ns; square symbols), followed by each optimisation step: (1) optimisation of background noise and detection efficiency ($\epsilon = 0.861$, $\lambda = 461$ kcps, $\rho = 0$ ns; diamond symbols), and (2) integration time adjustment for pile-up effects ($\epsilon = 0.861$, $\lambda = 461$ kcps, $\rho = 5.6$ ns; circle symbols). Cross symbols represent experimental data.

Appendix B. DMI 4-ring digitizer optimisation

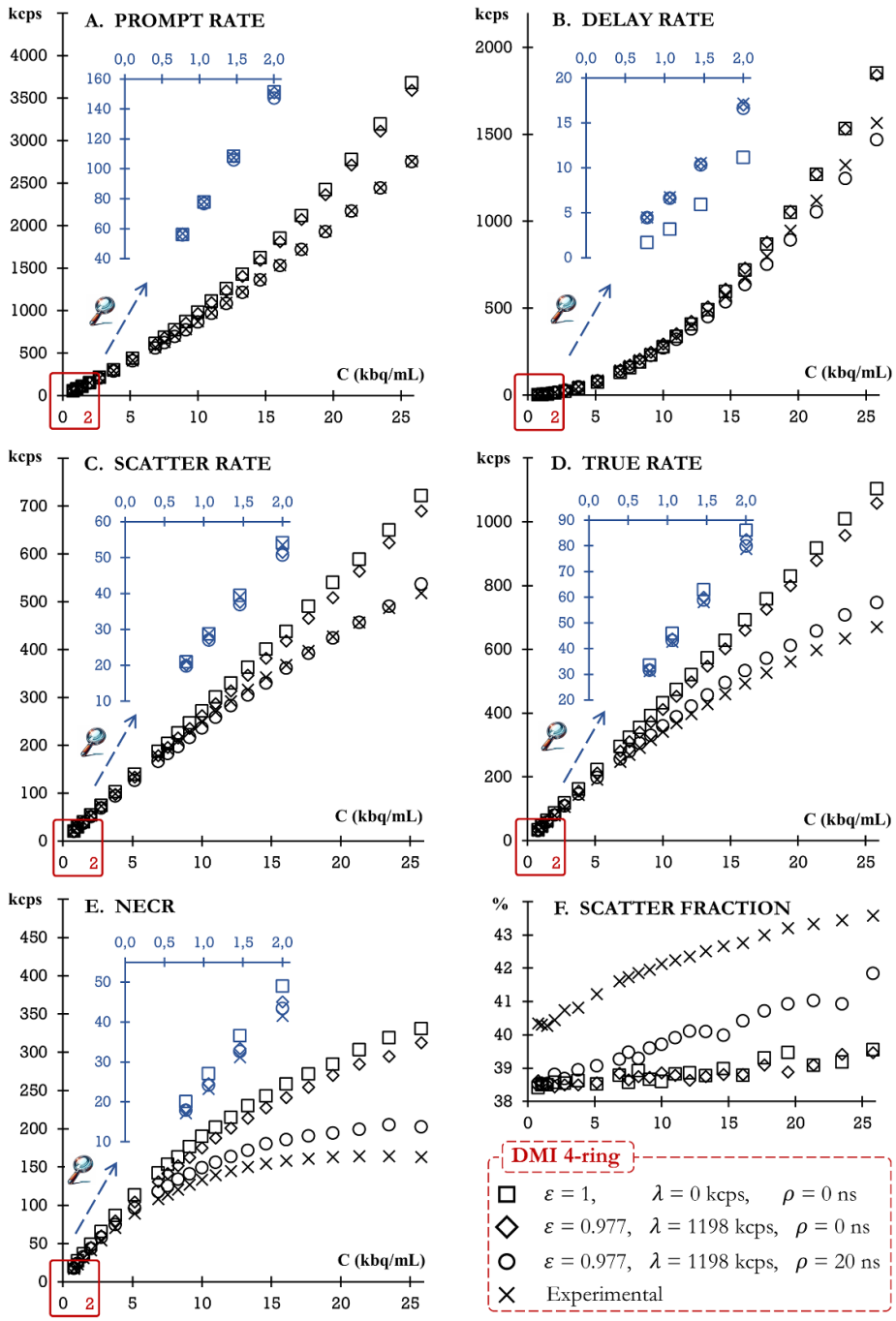

Figure B1. Simulated prompt, delay, scatter, true, NEC rates, and scatter fraction for the DMI 4-ring system without optimisation ($\epsilon = 1$, $\lambda = 0$ kcps, $\rho = 0$ ns; square symbols), followed by each optimisation step: (1) optimisation of background noise and detection efficiency ($\epsilon = 0.977$, $\lambda = 1198$ kcps, $\rho = 0$ ns; diamond symbols), and (2) integration time adjustment for pile-up effects ($\epsilon = 0.977$, $\lambda = 1198$ kcps, $\rho = 20$ ns; circle symbols). Cross symbols represent experimental data.

ORCID iDs

Julien Salvadori https://orcid.org/0000-0002-3823-2531
Ane Etxebeste https://orcid.org/0000-0001-6280-9268
Jean-Marc Vrigneaud https://orcid.org/0000-0002-3441-7520
David Sarrut https://orcid.org/0000-0002-4854-4141

References

Aklan B, Jakoby B W, Watson C C, Braun H, Ritt P and Quick H H 2015 Gate Monte Carlo simulations for variations of an integrated PET/MR hybrid imaging system based on the biograph MMR model *Phys. Med. Biol.* **60** 4731

Allison J *et al* 2016 Recent developments in GEANT4 *Nucl. Instrum. Methods Phys. Res.* A **835** 186–225

Brasse D, Kinahan P, Lartizien C, Comtat C, Casey M and Michel C 2005 Correction methods for random coincidences in fully 3D whole-body pet: Impact on data and image quality *J. Nucl. Med.* **46** 859–67

Frach T, Prescher G, Degenhardt C, de Gruyter R, Schmitz A and Ballizany R 2009 The digital silicon photomultiplier - principle of operation and intrinsic detector performance *2009 IEEE Nuclear Science Symp. Conf. Record (NSS/MIC)* pp 1959–65

GE Healthcare 2016 Discovery MI with lightburst digital 4-ring detector (Accessed 19 June 2024)

Geramifar P, Ay M, Shamsaie Zafarghandi M, Sarkar S, Loudos G and Rahmim A 2011 Investigation of time-of-flight benefits in an LYSO-based PET/CT scanner: a Monte Carlo study using GATE *Nucl. Instrum. Methods Phys. Res.* A **641** 121–7

Gonias P *et al* 2007 Validation of a GATE model for the simulation of the siemens biograph 6 PET scanner *Nucl. Instrum. Methods Phys. Res.* A **571** 263–6

Guez D, Bataille F, Comtat C, Honore P-F, Jan S and Kerhoas S 2008 Counting rates modeling for PET scanners with GATE *IEEE Trans. Nucl. Sci.* **55** 516–23

Gundacker S and Heering A 2020 The silicon photomultiplier: fundamentals and applications of a modern solid-state photon detector *Phys. Med. Biol.* **65** 17TR01

Herald M, Nicusan A, Wheldon T K, Seville J and Windows-Yule C 2022 Autonomous digitizer calibration of a Monte Carlo detector model through evolutionary simulation *Sci. Rep.* **12** 19535

Hsu D, Ilan E, Peterson W, Uribe J, Lubberink M and Levin C 2017 Studies of a next generation silicon-photomultiplier-based time-of-flight PET/CT system *J. Nucl. Med.* **58** 1511–8

Kalaitzidis P, Gustafsson J, Hindorf C and Ljungberg M 2022 Validation of a computational chain from pet Monte Carlo simulations to reconstructed images *Heliyon* **8** e09316

Lamare F, Turzo A, Bizais Y, Rest C C L and Visvikis D 2006 Validation of a Monte Carlo simulation of the philips allegro/GEMINI PET systems using GATE *Phys. Med. Biol.* **51** 943–62

Merlet A, Presles B, Su K-H, Salvadori J, Sayah Fand Jozi H, Cochet A and Vrigneaud J-M 2024 Validation of a discovery MI 4-ring model according to the NEMA NU 2-2018 standards: from Monte Carlo simulations to clinical-like reconstructions *EJNMMI Phys.* **11** 13

Moraes E R, Poon J K, Balakrishnan K, Wang W and Badawi R D 2015 Towards component-based validation of gate: aspects of the coincidence processor *Phys. Medica* **31** 43–48

NEMA 2018 NEMA standards publication NU 2-2018. Performance measurements of positron emission tomographs National Electrical Manufacturers Association (NEMA), Rosslyn, USA

Nikolopoulos D, Kottou S, Chatzisavvas N, Argyriou X, Vlamakis E, Yannakopoulos P and Louizi A 2013 A GATE simulation study of the siemens biograph DUO PET/CT system *Open J. Radiol.* **03** 56–65

Rausch I, Ruiz A, Valverde-Pascual I, Cal-González J, Beyer T and Carrio I 2019 Performance evaluation of the vereos PET/CT system according to the NEMA NU2-2012 standard *J. Nucl. Med.* **60** 561–7

Reddin J S, Scheuermann J S, Bharkhada D, Smith A M, Casey M E, Conti M and Karp J S 2018 Performance evaluation of the SiPM-based siemens biograph vision PET/CT system *2018 IEEE Nuclear Science Symp. and Medical Imaging Conf. Proc. (NSS/MIC)* pp 1–5

Salvadori J, Labour J, Odille F, Marie P-Y, Badel J-N, Imbert L and Sarrut D 2020 Monte Carlo simulation of digital photon counting PET *EJNMMI Phys.* **7** 23

Salvadori J, Odille F, Karcher G, Marie P-Y and Imbert L 2021 Fully digital PET is unaffected by any deterioration in TOF resolution and TOF image quality in the wide range of routine PET count rates *EJNMMI Phys.* **8** 1

Sarrut D *et al* 2021 Advanced Monte Carlo simulations of emission tomography imaging systems with GATE *Phys. Med. Biol.* **66** 10TR03

Sarrut D *et al* 2022 The OpenGATE ecosystem for Monte Carlo simulation in medical physics *Phys. Med. Biol.* **67** 184001

Schaart D R, Charbon E, Frach T and Schulz V 2016 Advances in digital sipms and their application in biomedical imaging *Nucl. Instrum. Methods Phys. Res.* A **809** 31–52

Schmidtlein C R *et al* 2005 Validation of GATE Monte Carlo simulations of the GE advance/discovery LS PET scanners: validation of GATE simulations of GE PET scanners *Med. Phys.* **33** 198–208

Stearns C W, McDaniel D L, Kohlmyer S G, Arul P R, Geiser B P and Shanmugam V 2003 Random coincidence estimation from single event rates on the Discovery ST PET/CT scanner *IEEE Nuclear Science Symp. Conf. Record* vol **5** pp 3067–9

Strydhorst J and Buvat I 2016 Redesign of the gate pet coincidence sorter *Phys. Med. Biol.* **61** N522–31

Tiwari A, Merrick M, Graves S A and Sunderland J 2022 Monte Carlo evaluation of hypothetical long axial field-of-view PET scanner using GE discovery MI PET front-end architecture *Med. Phys.* **49** 1139–52

Trindade A *et al* 2012 Validation of GATE Monte Carlo simulations of the philips GEMINI TF and TruFlight select PET/CT scanners based on NEMA NU2 standards *2012 IEEE Nuclear Science Symp. and Medical Imaging Conf. Record (NSS/MIC)* (IEEE) pp 2546–9

van Sluis J, de Jong J, Schaar J, Noordzij W, van Snick P, Dierckx R, Borra R, Willemsen A and Boellaard R 2019 Performance characteristics of the digital biograph vision PET/CT system *J. Nucl. Med.* **60** 1031–6

Wagadarikar A A, Iván A, Dolinsky S and McDaniel D L 2014 Sensitivity improvement of time-of-flight (TOF) pet detector through recovery of compton scattered annihilation photons *IEEE Trans. Nucl. Sci.* **61** 121–5

Zein S, Karakatsanis N, Conti M and Nehmeh S 2020 Monte Carlo simulation of the siemens biograph visiontm pet with extended axial field-of-view using sparse detector module rings configuration *IEEE Trans. Radiat. Plasma Med. Sci.* pp 1–1

Zhang J, Maniawski P and Knopp M 2018 Performance evaluation of the next generation solid-state digital photon counting PET/CT system *EJNMMI Res.* **8** 97